Tungsten evolution under helium irradiation: Shape of bubbles by TEM and in-situ GISAXS analysis

L. Corso, S. Curiotto, E. Bernard, Martiane Cabie, C. Martin, Lucio Martinelli, Fabien Cheynis, Pierre Müller, Frédéric Leroy

▶ **To cite this version:**

L. Corso, S. Curiotto, E. Bernard, Martiane Cabie, C. Martin, et al.. Tungsten evolution under helium irradiation: Shape of bubbles by TEM and in-situ GISAXS analysis. Nuclear Materials and Energy, 2023, 37, pp.101533. 10.1016/j.nme.2023.101533 . hal-04257914

HAL Id: hal-04257914
https://hal.science/hal-04257914

Submitted on 25 Oct 2023

HAL is a multi-disciplinary open access archive for the deposit and dissemination of scientific research documents, whether they are published or not. The documents may come from teaching and research institutions in France or abroad, or from public or private research centers.

L'archive ouverte pluridisciplinaire **HAL**, est destinée au dépôt et à la diffusion de documents scientifiques de niveau recherche, publiés ou non, émanant des établissements d'enseignement et de recherche français ou étrangers, des laboratoires publics ou privés.

Distributed under a Creative Commons Attribution 4.0 International License

Nuclear Materials and Energy 37 (2023) 101533

Contents lists available at ScienceDirect

Nuclear Materials and Energy

journal homepage: www.elsevier.com/locate/nme

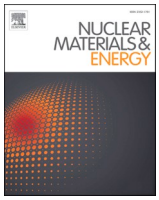

Tungsten evolution under helium irradiation: Shape of bubbles by TEM and in-situ GISAXS analysis

L. Corso [a,b,*], S. Curiotto [b], E. Bernard [a], M. Cabie [c], C. Martin [d], L. Martinelli [e], F. Cheynis [b], P. Muller [b], F. Leroy [b]

[a] CEA, IRFM, F-13108 Saint Paul-lez-Durance, France
[b] Aix Marseille Université, CNRS, CINAM, Marseille, France
[c] Aix Marseille Univ., CNRS, Centrale Marseille, FSCM (FR1739), CP2M, Marseille, France
[d] Aix Marseille Univ., CNRS, PIIM, UMR 7345, Marseille, France
[e] Institut Néel CNRS/UGA UPR2940, 38000 Grenoble, France

ARTICLE INFO

Keywords:
Tungsten
Helium
Microstructure evolution
Bubbles
GISAXS
Equilibrium shape

ABSTRACT

The evolution of the tungsten microstructure and properties under helium irradiation could cause problems for both operational and safety reasons in fusion reactors. In particular, the presence of helium bubbles, formed mainly in the subsurface area, modifies the mechanical and retention properties of radioactive elements. In that context we have investigated the shape of helium bubbles in tungsten induced by helium irradiation under well-defined experimental conditions. We have used single crystals with controlled bombardment energy, flux, fluence and post-irradiation annealing at high temperature under ultra-high vacuum in order to get closer to the thermodynamic equilibrium of the helium bubbles. The bubble shape has been characterized by a combination of TEM and 3D reciprocal space map by in-situ GISAXS. We have shown the presence of facetted bubbles exposing {1 1 0} and {1 0 0} facets of similar size. Using Wulff theorem and experimental results from both techniques, we derive a surface energy ratio of $\frac{\gamma_{100}}{\gamma_{110}} = 1.03 \pm 0.03$.

Introduction

Nuclear fusion, as a carbon-free energy source, is actively pursued by the international community. In tokamaks, the confinement is obtained through intense magnetic fields, but some plasma ions escape the magnetic confinement and interact with the first physical barrier, the plasma-facing materials that constitute the first wall [1]. This wall and in particular the divertor plays a key role by extracting the excess of heat and particles and is a key component in the fusion reactor efficiency. However, this irradiation can lead to important damages at the surface and deeper in the bulk, affecting the properties and life span of the materials, and essentially the efficiency of the reactor [2]. Tungsten (W) has been chosen for some of the most recent fusion reactors (ITER [3], WEST [4]) as the material of the divertor exposed to the most intense flux of particles such as deuterium, tritium and helium (He) ions, neutrons and heat. The ITER divertor could reach 1573 K in normal operation [3] and up to 2273 K in off-normal operation. Transmutation elements and displacement damage caused by neutron irradiation alter the plasma facing properties of W materials. For instance it has been shown an increase of hardening and electrical resistivity [5–7]. The charge-exchange neutrals are expected to irradiate the divertor with only low energy (<20 eV) [8], therefore they should not penetrate deep and should not lead to sputtering, as the threshold displacement energy of W is much higher (~90 eV [9]). The interaction with He has been proven to significantly affect the surface, with the observed formation of bubbles, or W-nanotendrils (so-called fuzz) in the material [10–12]. These changes at the material surface, particularly the He bubbles, can modify the thermal and mechanical properties and increase tritium retention in the material [13,14]. These alterations are identified as a major issue for next generation reactors. Understanding He impact on W properties as a plasma-facing material is therefore of considerable importance.

In a tokamak environment, the study the He/W interaction to address the atomic mechanisms responsible for bubbles formation is very complex. Indeed, several parameters are difficult to control separately as temperature, implantation energy, flux, fluence,

* Corresponding author at: CEA, IRFM, F-13108 Saint Paul-lez-Durance, France.
E-mail address: loic.corso@cea.fr (L. Corso).

https://doi.org/10.1016/j.nme.2023.101533
Received 30 June 2023; Received in revised form 28 September 2023; Accepted 9 October 2023
Available online 13 October 2023
2352-1791/© 2023 The Author(s). Published by Elsevier Ltd. This is an open access article under the CC BY-NC-ND license (http://creativecommons.org/licenses/by-nc-nd/4.0/).

contamination… Hence, significant theoretical and computational efforts have been made. Several research groups have performed a variety of atomistic simulations on He interaction with W over the last ten years. These studies include the He bubble formation and growth, both in bulk [15–22] and near surfaces [23,24] as well as the He interaction with grain boundaries and surfaces [15,25–27]. Such simulations are crucial to address W evolution in future fusion devices however their validation through well-controlled experiments is now mandatory.

Until now the experimental studies on He bubbles in W have been performed using a wide range of parameters (manufacturing parameters, polycrystalline material, large/low defect content, oxidized W surface, non-controlled atmosphere, different temperature…) that make the results and interpretation of the basic mechanisms of the microstructure evolution questionable. For instance it has been reported that the shape of He bubble is spherical [28,29] or faceted [30–32] in W depending on the temperature [33]. Results on polycrystalline W are partially in disagreement:

(i) Harrison et al. [34] have reported that He implantation at 773 K, 1073 K and 1273 K forms non facetted He-bubbles.
(ii) {1 1 0} facets are observed in polycrystalline W, implanted and annealed up to 1273 K [35]. Similarly Ialovega and co-workers [36] have proposed a 3D shape of bubbles composed exclusively of {1 1 0} facets after He implantation at 1073 K and annealing up to 1350 K.
(iii) More recently Bergstrom et al. [37] have compared in details density functional theory (DFT) calculations and transmission electron microscopy (TEM) images of small bubbles (<5 nm diameter) in a polycrystalline sample implanted at 1223 K. They conclude on a more complex shape composed of {1 1 0}, {1 1 1}, {0 1 3} and {1 1 2} facets. The differences among the literature results are probably inherent to different implantation conditions and to non-controlled parameters used for He implantation in W.

In addition, TEM technique does not provide a statistical view of the sample that makes the detection of all the facets questionable. Grazing incidence small angle x-ray scattering (GISAXS) is a well-established, non-destructive and complementary technique to TEM for the investigation of thin films, surface and subsurface structures [38]. Using this technique, the shape and size of nanostructures can be measured providing much greater statistical information than with TEM. Thompson and coworkers have characterized post-mortem polycrystalline W samples exposed to He plasma in the research facilities PISCES-B, MAGPIE and in the Large Helical Device (LHD). Spherical bubbles with bimodal distribution of the diameter in the range of 1.5 to 5 nm and located in the first 31 nm below the material surface are reported for He implantation at 973 K in PISCES-B [39]. GISAXS and TEM analysis are in agreement for the characterization of samples exposed to a He plasma in the LHD at 1073 K, where spheroidal bubbles with average diameter of 0.6 nm have been reported [40].

In this context we propose to characterize He bubbles in W using nanoscience methods and techniques. Our approach is based on He implantation in single-crystalline W under well-controlled experimental conditions in combination with TEM/GISAXS measurements to address the shape of He bubbles. In that purpose we have worked under UHV environment to avoid contamination. He bombardment is performed at a well-defined energy (2 keV). The annealing temperature is sufficiently high (1773 K) to be representative of the ITER divertor temperature and enhancing atomic diffusion to approach the thermodynamic equilibrium shape of He bubbles.

Experimental protocols

Single-crystalline W samples (purity greater than 99.999 %) oriented {1 0 0}, {1 1 0} and {1 1 1} consist of disk-shaped specimens with 9 mm diameter and a thickness of 1 mm. Samples with an orientation accuracy below 0.1° and polished with surface roughness below 0.01 μm where purchased from MaTeck. The surface preparation procedure is fully described in [41]. Briefly, it consists in annealing the W crystals at 1273 K under a O_2 partial pressure of 10^{-6} mbar to remove carbon impurities and high temperature ultra-high vacuum (UHV) flash up to 2273 K to remove the remaining tungsten oxide layer. The level of contamination is checked to be below the detection limit of Auger electron spectroscopy (AES). The flatness of the samples surface is also controlled by low-energy electron microscopy (LEEM) to decrease the background signal when performing GISAXS measurements. Finally, a 5 nm Au layer is deposited on top of the surface to avoid contamination during transportation to the European synchrotron radiation facility (ESRF) for He bombardment and GISAXS studies.

Prior the He bombardment, the Au layer is removed by heating the samples to 1100 °C under UHV. The Au desorption is monitored by grazing incident X-ray diffraction (GIXD) to ensure that no Au remains on the surface. Samples are crystallographically oriented by GIXD. Both GISAXS/GIXD measurements and ion implantation of He at 2 keV have been performed at the ESRF in the INS2 set up of the BM32 beamline.

The principle of GISAXS measurements is presented in the scheme of the Fig. 1. $\mathbf{k_i}$ and $\mathbf{k_f}$ are defined as incident and scattered X-ray wave vectors, with $|k_i| = |k_f| = \frac{2\pi}{\lambda} = k_0$, α_i and α_f are the incident and exit out-of-plane angles, $2\theta_f$ is the in-plane scattering angle and ω is the azimuthal angle. Scattering of X-ray on the sample is defined by the wave vector transfer $\mathbf{q} = \mathbf{k_f} - \mathbf{k_i}$.

The right part of the Fig. 1 shows a 3D iso-intensity surface map of the reconstructed reciprocal space. It corresponds to a set of 150 GISAXS patterns recorded over an angular range in ω of 150° (1° degree angular step) at constant incident angle α_i (0.6°).

GISAXS measurements were performed at 10 keV (wavelength λ = 0.124 nm), the detector is a charge-coupled device (CDD) camera composed of two modules. The dead zone visible on the recorded patterns is the gap between those two modules. The sample-camera distance was 802 mm for W(1 1 0) and W(1 0 0) and 1246 mm for W(1 1 1). The X-ray incident angles αi were between 0.2°, and 0.6°, i.e. below and above the critical angle of total external reflexion (0.4°) in order to tune the penetration depth of the X-ray beam. At incident angle equal to 0.6° the maximum of X-ray penetration depth is 40.7 nm. The applied He flux is $2.4\text{x}10^{17}$ He.m^{-2}.s^{-1} and the reached fluence is $1.0\text{x}10^{22}$ He.m^{-2}. The samples temperature was maintained at 1273 K during He bombardment. After He implantation, all crystals were heated up to 1773 K during 20 min in UHV while characterizing the bubble morphology and size by GISAXS. After He implantation and UHV annealing, thin lamellae for TEM analysis were fabricated by focused ion beam (FIB) using a FEI Helios 600 Nanolab Dual Beam. A protective layer of platinum (Pt) is deposited on the surface of the cutting area to prevent the degradation of the bubble zone. TEM analysis is performed with a Jeol JEM-2100F apparatus. The surface of the samples is also analysed by scanning electron microscopy (SEM) using a JEOL JSM-7900F.

Results

TEM analysis: Shape determination of He bubbles in W

TEM analysis reveals He-bubbles in the first 40 nm deep area of all the samples. The shape of the bubbles is facetted, and does not depend on the bubble size, nor on the crystallographic orientation of the sample surface. Spherical bubbles have not been observed. In Fig. 2a is presented a TEM image of He-bubbles in W(1 0 0) close to the [0 0 1] zone axis as shown by the diffractogram in the inset. We can see that the large bubbles show a preferential elongation in one direction that is attributed to bubbles coalescence. Bubbles are composed of {1 1 0} and {1 0 0} planes forming an octagonal shape as similarly found by Goodhew and Tyler in other bcc metals or alloys [42]. Previous observations of other authors also mention {1 1 0} planes to compose the surface of facetted

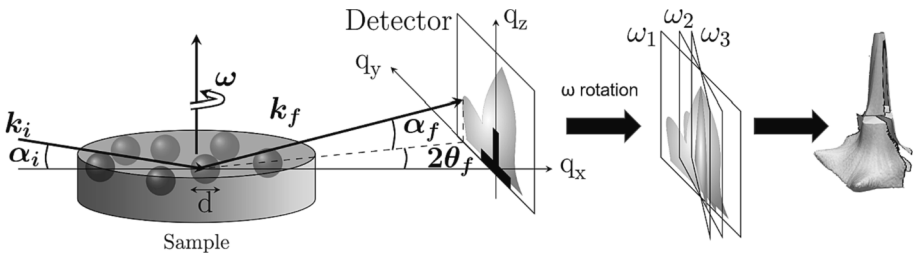

Fig. 1. Schematic of the GISAXS geometry. Incident and scattered X-rays are defined respectively by the wave vectors $\mathbf{k_i}$ and $\mathbf{k_f}$, the incident angle α_i is set in the range 0.2° to 1°. α_f and $2\theta_f$ are respectively the scattering out-of-plane and in-plane angles. ω is the azimuthal angle that defines the probing direction. The right part is a 3D iso-intensity surface map obtained from the compilation of 2D patterns recorded after azimuthal rotation.

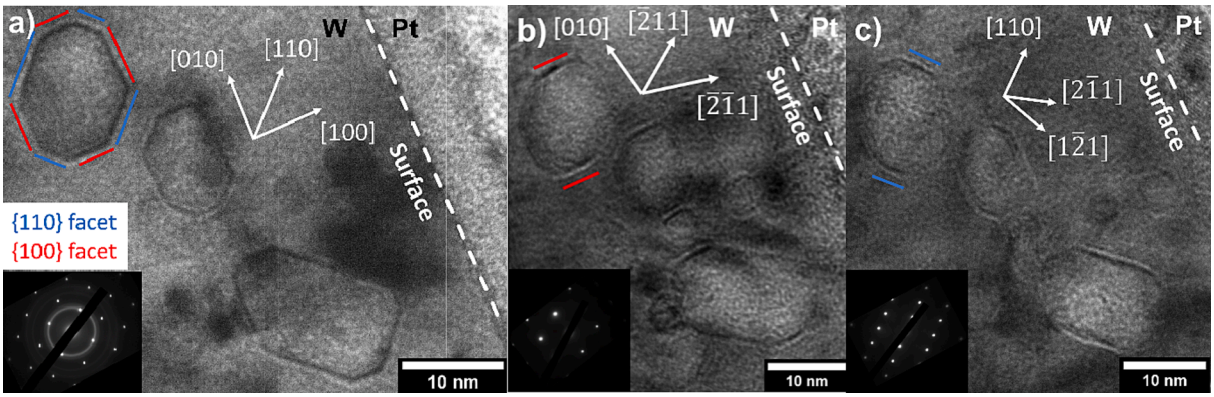

Fig. 2. Bright-field TEM Images of He implanted W(1 0 0) annealed up to 1773 K. The three images are taken in the same area from close to the [0 0 1] zone axis (a), close to the [1 0 2] zone axis (b) and close to the [$\bar{1}$13] zone axis (c). Facetted He-bubbles are composed of {1 1 0} and {1 0 0} facets (in blue and red respectively). Diffractograms are shown in the insets, rings are due to polycrystalline platinum (Pt) deposited on the W surface. (For interpretation of the references to colour in this figure legend, the reader is referred to the web version of this article.)

bubbles [35–37]. However, {1 0 0} planes have never been mentioned in those studies even though they could minimize the surface energy of bubbles as discussed in the next section. We do not detect other planes, indicating that all other {hk0}-facets are absent (e.g. {2 1 0}, {3 1 0}). In Fig. 2b is shown the same area close to the [102] zone axis. The {1 0 0} plane at the surface of the bubbles is again visible. However, the bubble edge is rounded everywhere else. This result indicates that $\{h2k\bar{k}\}$-type facets with $h \neq 0$ are absent (e.g $\{12\bar{1}\}$, $\{22\bar{1}\}$, …). At last Fig. 2c shows a TEM micrograph considering the [$\bar{1}$13] zone axis. The {1 1 0} facets are visible, but again the other parts of the edges are rounded indicating no other facet exists with normal vector perpendicular to the [$\bar{1}$13] direction (e.g. {3 0 1}, $\{2\bar{1}1\}$, …). Similarly, only {1 0 0} and {1 1 0} facets are observed for W(1 1 0) and W(1 1 1).

We have measured the facet length of at least 15 bubbles per sample. We have chosen bubbles with diameter larger than 5 nm to clearly see the facet limits. The sizes of {1 1 0} and {1 0 0} facets measured by TEM in [0 0 1] zone axis for each sample are shown in Fig. 3. The average size of {1 1 0} and {1 0 0} facets follow the same tendency observed in [35,43] for lower fluence and temperature conditions. However, the measurements show a very disperse distribution. The standard deviations and the mean of the distributions are of the same order due to the low statistics achievable by TEM technique.

GISAXS analysis: Statistical study of the He-bubbles facets

GISAXS measurements were performed to have a statistically significant determination of all the facets present at the internal surface of the He bubbles. To probe all possible crystallographic orientations of facets, GISAXS patterns were measured at different azimuths for all three W single crystals, i.e. by rotating the sample around the normal to the surface. Fig. 4 shows iso-intensity surface maps for implanted W(1 0 0), W(1 1 0) and W(1 1 1) single crystals and recorded after annealing up to 1773 K and some particular GISAXS patterns at different azimuth angles (ω angle).

The iso-intensity surface maps show lateral streaks highlighted with red arrows and red ellipses in precise directions of the reciprocal space. These diffuse scattering streaks result from the truncation of the bubbles by well-defined planes corresponding to facets [38]. The inclination angle between the diffuse scattered intensity and the surface normal depends on the relative orientation of the facets with the surface of the single crystal (e.g. 45° for {1 1 0} facets on (1 0 0)-oriented W).

The origin of these lateral streaks has been investigated by varying the incident angle α_i. When α_i decreases down to 0.4° and 0.2°, the surface contribution is enhanced while the contribution from buried bubbles decreases. In these conditions the intensity of all lateral streaks, except the twin streak visible in the white ellipse on Fig. 4b, tend to disappear. Thus, the lateral streaks are attributed to buried bubbles facets. As seen by TEM, two types of facets exist at the bubbles surface: the {1 0 0} and the {1 1 0} facets. We have not observed streaks corresponding to bubble facets other than {1 0 0} and {1 1 0} ones. In addition, no spherical bubbles are observed as no 3D isotropic scattering is recorded.

In the case of W(1 0 0) the X-ray diffuse scattering on {1 0 0} facets is expected to produce scattering rods at 90° with respect to the vertical ($\alpha_f = 0°$) which is located below the critical angle that defines the limit where intensity can be transmitted. Hence, {1 0 0} facet on W(1 0 0) cannot be measured. On W(1 1 0) a twin lateral scattering rod of {1 0 0}-type is visible (see white ellipse in GISAXS pattern of Fig. 4). This doubling effect is due to multiple scattering processes occurring at the sample surface and below the surface that can be described within the Distorted Wave Born Approximation (DWBA) [38]. It combines X-ray diffuse scattering due to holes formed at the surface by bubble bursting

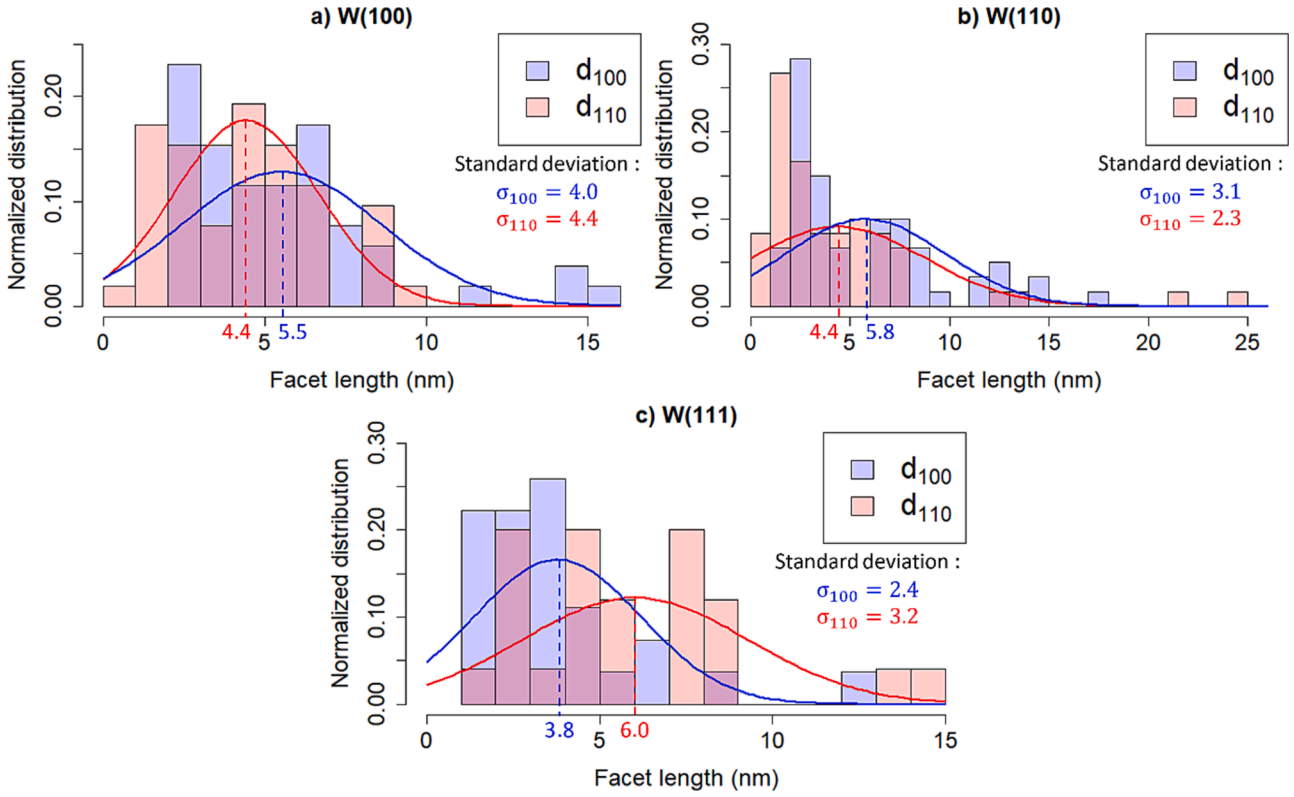

Fig. 3. TEM measurements of the facet lengths of He bubbles in W using [0 0 1] zone axis. {1 0 0} facet in blue and {1 1 0} facet in red, in W(1 0 0) (a), W(1 1 0) (b) and W(1 1 1) (c).The length distribution is fitted by a Gaussian function in blue for {1 0 0} facet and red for {1 1 0} facet. The standard deviation and the mean of the distribution are shown for all facets. (For interpretation of the references to colour in this figure legend, the reader is referred to the web version of this article.)

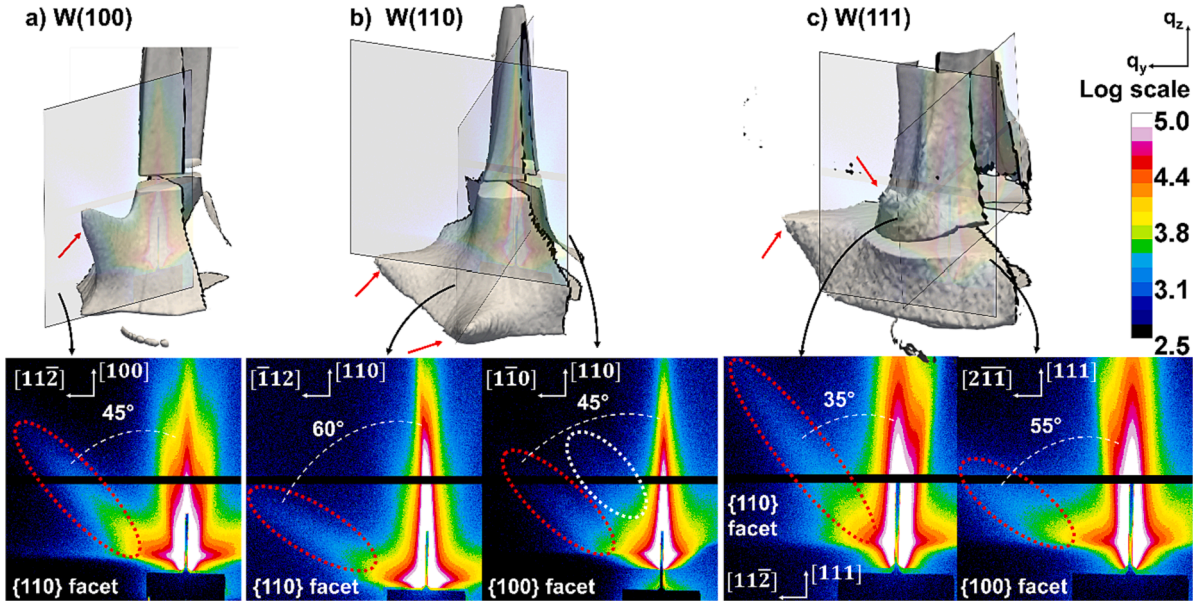

Fig. 4. a) Reconstruction of iso-intensity surface map of W(1 0 0),b) W(1 1 0) and c) W(1 1 1) recorded during azimuthal scan at $\alpha_i = 0.6°$, after 2 keV He implantation and UHV annealing up to 1773 K. Below: particular GISAXS patterns corresponding to a cut of the 3D map. Lateral rods on GISAXS patterns are due to X-ray scattering on He-bubbles facets (red dashed circle). Corresponding facets are {1 1 0} and {1 0 0}. On W(1 1 0) (b) the twin rod of {1 0 0}-type facet (white dashed circle) is due to multiple scattering on surface morphologies and buried bubble internal surface. (For interpretation of the references to colour in this figure legend, the reader is referred to the web version of this article.)

and also buried bubbles. Indeed, as shown by scanning electron microscopy (SEM) in Fig. 5 the surface of W(1 1 0) is not flat. Holes due to bubbles bursting, appearing in black on the SEM micrograph, pave the surface. In addition, elongated surface structures due to surface healing are observable. Similar morphologies have also been observed in [36,44].

The average size *d* of a facet can be deduced measuring the full width at half maximum (FWHM) of the diffuse scattering streak of the corre-

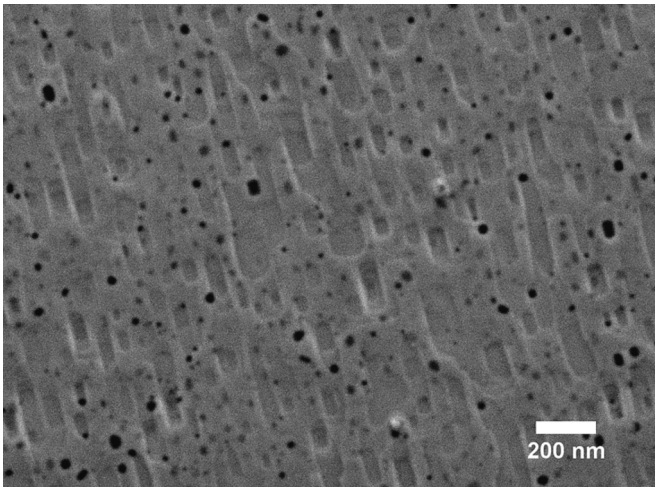

Fig. 5. SEM micrograph of W(1 1 0) surface after 2 keV He implantation and UHV annealing up to 1773 K. Surface healing is occurring as shown by aligned rectangular reconstruction structures. Black dots correspond to holes formed by bubbles bursting.

sponding facet noted Δq and approximated as:

$$d = \frac{2\pi}{\Delta q}$$

In Table 1 the sizes d of {1 1 0} and {1 0 0} facets measured by GISAXS for each W crystals are shown (except for W(1 0 0) where only the {1 1 0} facet can be measured). The uncertainty on the measurement is mostly due to the fit quality of the intensity profile along the streak width. In our case, the uncertainty on the sizes d is evaluated at maximum 5% of the measured length. The average length of the facets measured by GISAXS is then much more precise than by TEM and thus more adequate to establish the general shape of the bubbles. In the following only GISAXS measurements will be considered to address the bubble shape.

Discussion

The experimental equilibrium shape of bubbles in W

The Wulff theorem [45] predicts the equilibrium shape of objects (crystals or voids in crystals) by minimizing the total surface energy of a given volume. In crystals, due to surface energy anisotropy, facets of well-defined crystallographic orientations are formed to minimize the total surface energy. The Wulff theorem shows that the surface energy of a plane (γ_{hkl}) is proportional to the distance h_{hkl} from the centre of the bubble to this facet:

$$\gamma_{100} = h_{100}.C$$

$$\gamma_{110} = h_{110}.C$$

where C is a constant independent of the volume of the bubble. For a cubic lattice structure, the distances h_{100} and h_{110} are related to the facet length d_{100} and d_{110} (defined in Fig. 6) through:

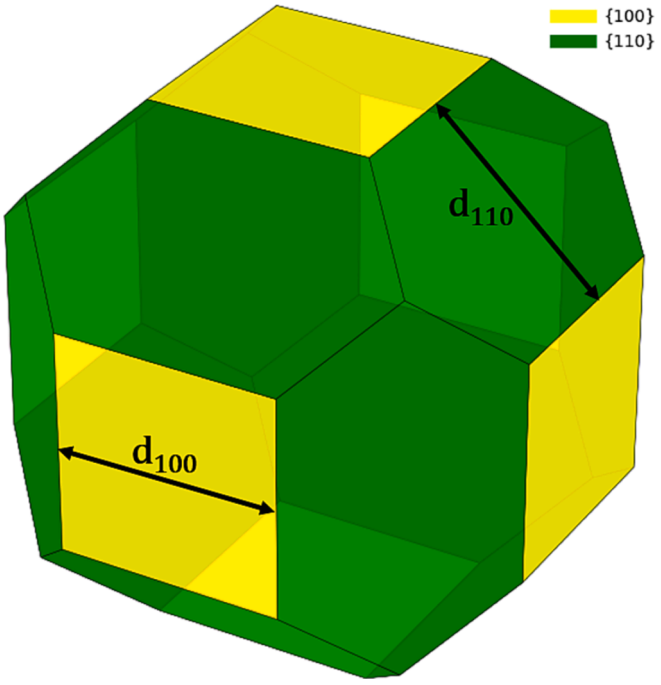

Fig. 6. Wulff construction generated by the energetic ratio deduced by GISAXS. Black arrows represent the lengths used in the energetic ratio calculation.

$$h_{100} = \frac{d_{100}}{2} + \frac{d_{110}}{\sqrt{2}}$$

$h_{110} = \frac{d_{100}}{\sqrt{2}} + \frac{d_{110}}{2}$ Hence the energy ratio between {1 0 0} and {1 1 0} facets can be deduced from the size of those facets:

$$\frac{\gamma_{100}}{\gamma_{110}} = \frac{d_{100}+\sqrt{2}d_{110}}{\sqrt{2}d_{100}+d_{110}}$$

The ratio of d_{100} and d_{110} provides the $\frac{\gamma_{100}}{\gamma_{110}}$ energetic ratio from which we can deduce the Wulff shape of the He bubbles and compare it with the literature results. In Table 2 is shown a summary of the $\frac{\gamma_{100}}{\gamma_{110}}$ energetic ratio obtained by GISAXS. We can evaluate the $\frac{\gamma_{100}}{\gamma_{110}}$ ratio as 1.03 ± 0.03 by GISAXS. The simulated Wulff bubble shape corresponding to this ratio is given in Fig. 6, the visualisation is performed using the Wulffpack software [46].

The simulated equilibrium shape of bubbles in W

Our experimental result can be compared with the literature. Density Functional Theory (DFT) [37,47–49] or Molecular dynamics (MD) [50,51] simulations have been used to calculate the surface energy of different orientations of W crystals. Fig. 7 combines different energetic ratios $\frac{\gamma_{hkl}}{\gamma_{110}}$ determined from the literature and the deduced Wulff shapes. A large discrepancy between the values has been found, corresponding

Table 1
GISAXS measurement of facet length of bubbles in W(1 0 0), W(1 1 0) and W (1 1 1) after 2 keV implantation at 1273 K and annealed up to 1773 K.

Sample	Average length of facet by GISAXS (in nm)	
	d_{110}	d_{100}
W(1 0 0)	9.1 ± 0.5	X
W(1 1 0)	11.3 ± 0.6	9.2 ± 0.5
W(1 1 1)	13.6 ± 0.7	12.2 ± 0.6

Table 2
The energetic ratio between surface (1 0 0) and (1 1 0) measured by GISAXS for W(1 0 0), W(1 1 0) and W(1 1 1).

Sample	$\frac{\gamma_{100}}{\gamma_{110}}$
W(1 0 0)	X
W(1 1 0)	1.04 ± 0.02
W(1 1 1)	1.02 ± 0.02

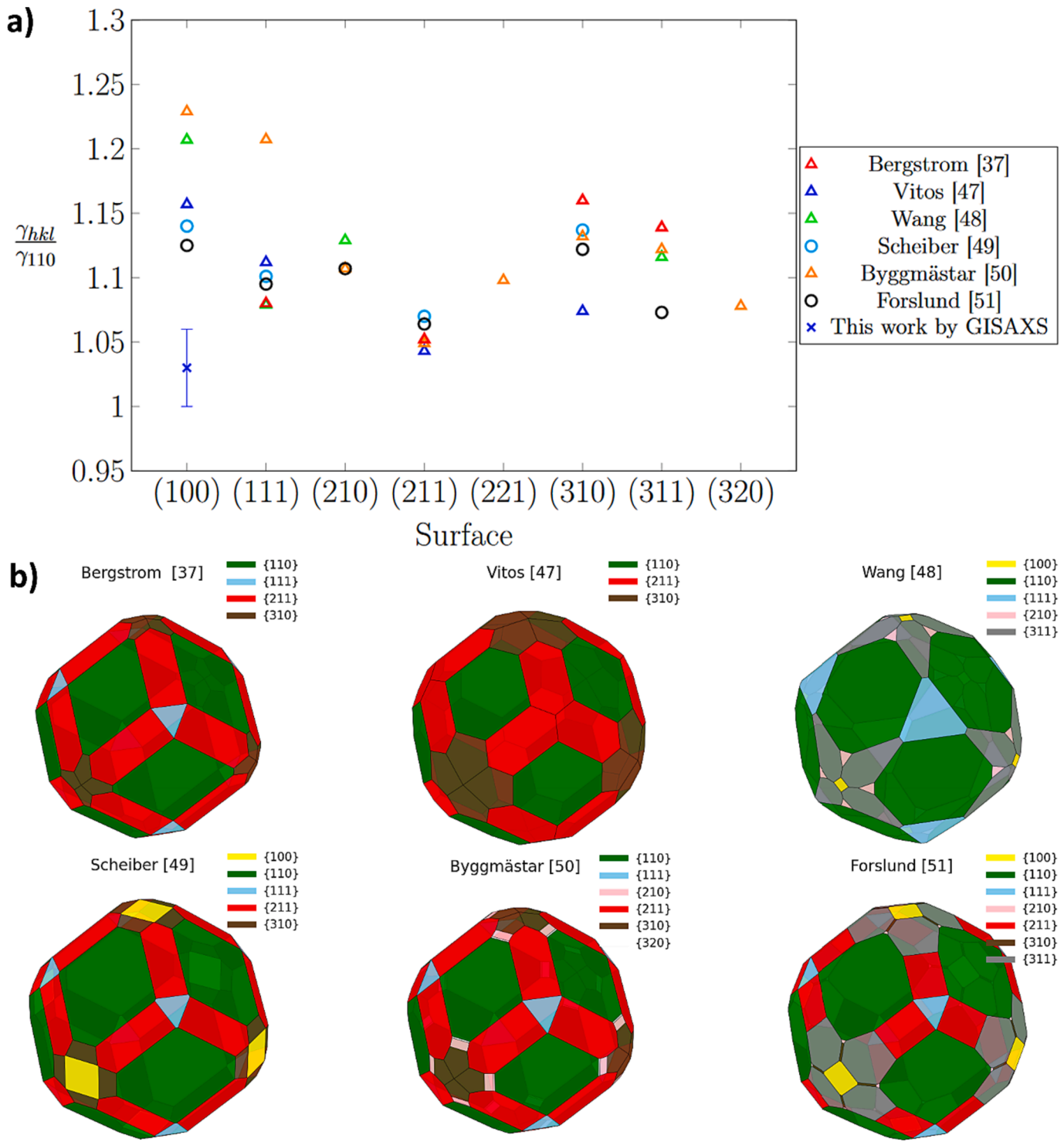

Fig. 7. a) Energetic ratio deduced by dft or md simulations for various surface orientations, circles are coupled approach considering temperature effect. b) wulff constructions generated using the energetic ratios of (a).

to very different expected bubble shapes. The studies coupling DFT to quasi-harmonic approximation (QHA) in [49] or MD in [51] aim at taking into account the effect of temperature on surface energies. In all cases, the {1 0 0} facet appears on the equilibrium shape generated at 1773 K. According to the literature the $\frac{\gamma_{100}}{\gamma_{110}}$ energetic ratio decreases as the temperature increases, therefore the {1 0 0} facet size is expected to increase with temperature. According to the calculations, the {2 1 1} is the second most dominant facet of the Wulff shape at 0 K, but it is reported to shrink when the temperature increases (see [49]). Therefore, the lack of {2 1 1} facets in our high-temperature experimental observations is not in disagreement with the simulations. Let us note that DFT simulations do not lead to a consensus, and that predicting an equilibrium shape at a given temperature from simulations performed at 0 K is delicate. Furthermore, most calculations neglect the W-He interaction. Recent approaches combining QHA-DFT [49] or MD-DFT [51] to take into account temperature dependence show a closer agreement to our experimental observations.

Conclusions

In conclusion, we have studied the shape of He bubbles in W by TEM and GISAXS. We have used well-controlled W samples in terms of crystallography, purity and defectuosity. Moreover, we have selected monokinetic He ion exposure conditions and performed high temperature annealing up to 1773 K under ultra-high vacuum environment to get closer to the equilibrium shape of the formed bubbles. By combining in situ GISAXS measurements with azimuthal scan and TEM cross section analysis we have found that the He bubbles are made exclusively of {1 1 0} and {1 0 0} facets. The deduced size of {1 1 0} and {1 0 0} facets is similar allowing us to estimate the surface energy ratio $\frac{\gamma_{100}}{\gamma_{110}} = 1.03 \pm 0.03$ with relatively low experimental uncertainty thanks to the GISAXS technique. We believe that these experimental results will be a basis for future theoretical work to better describe the He-bubble shape and formation processes, in the context of the development of fusion reactors. Finally, as the implantation energy is expected to be around 100 eV [8] in tokamaks, we aim at decreasing the implantation energy of He ions in future experiments to get closer to fusion relevant conditions.

CRediT authorship contribution statement

L. Corso: Conceptualization, Methodology, Formal analysis, Investigation, Writing – original draft. **S. Curiotto:** Formal analysis, Investigation, Writing – review & editing. **E. Bernard:** Formal analysis, Investigation, Resources, Writing – review & editing, Supervision. **M. Cabie:** Investigation, Writing – review & editing. **C. Martin:** Resources, Writing – review & editing. **L. Martinelli:** Investigation, Writing – review & editing. **F. Cheynis:** Writing – review & editing. **P. Muller:** Writing – review & editing. **F. Leroy:** Formal analysis, Investigation, Resources, Writing – review & editing, Supervision.

Declaration of Competing Interest

The authors declare that they have no known competing financial interests or personal relationships that could have appeared to influence the work reported in this paper.

Data availability

Data will be made available on request.

Acknowledgments

This work has been carried out within the framework of the EUROfusion Consortium, funded by the European Union via the Euratom Research and Training Programme (Grant Agreement No 101052200 — EUROfusion). Views and opinions expressed are however those of the author(s) only and do not necessarily reflect those of the European Union or the European Commission. Neither the European Union nor the European Commission can be held responsible for them. This work has been also carried out within the framework of the French Federation for Magnetic Fusion Studies (FR-FCM). In particular, we are grateful to D. Chaudanson and A. Altié for their help in SEM and TEM characterizations. We gratefully acknowledge the helpful discussions with Dr. T. Swinburne, Dr J Mougenot and Dr M-F Barthe.

References

[1] J. Roth, et al., J. Nucl. Mater. 390–391 (2009) 1.
[2] G. De Temmerman, T. Hirai, R.A. Pitts, Plasma Phys. Control. Fusion 60 (2018), 044018.
[3] R.A. Pitts, et al., Nucl. Mater. Energy 20 (2019), 100696.
[4] J. Bucalossi, et al., Fusion Eng. Des. 89 (2014) 907.
[5] R.C. Rau, J. Moteff, R.L. Ladd, J. Nucl. Mater. 24 (1967) 164.
[6] V. Barabash, G. Federici, M. Ro, J. Nucl. Mater. (2000).
[7] A. Hasegawa, et al., Fusion Eng. Des. 89 (2014) 1568.
[8] G. Federici, et al., Nucl. Fusion 41 (2001) 1967.
[9] M.J. Banisalman, S. Park, T. Oda, J. Nucl. Mater. 495 (2017) 277.
[10] M. Miyamoto, et al., J. Nucl. Mater. 463 (2015) 333.
[11] S. Kajita, et al., J. Nucl. Mater. 418 (2011) 152.
[12] D. Nishijima, et al., J. Nucl. Mater. 313–316 (2003) 97.
[13] M.J. Baldwin, et al., Nucl. Fusion 51 (2011), 129501.
[14] J. Roth, K. Schmid, Phys. Scr. T145 (2011), 014031.
[15] F. Sefta, et al., Nucl. Fusion 53 (2013), 073015.
[16] F. Sefta, N. Juslin, B.D. Wirth, J. Appl. Phys. 114 (2013), 243518.
[17] A.M. Ito, et al., Phys. Scr. T159 (2014), 014062.
[18] X.-C. Li, et al., J. Nucl. Mater. 455 (2014) 544.
[19] Y.L. Zhou, et al., J. Nucl. Mater. 446 (2014) 49.
[20] L. Sandoval, et al., Phys. Rev. Lett. 114 (2015), 105502.
[21] R. Kobayashi, et al., J. Nucl. Mater. 463 (2015) 1071.
[22] L. Hu, et al., J. Appl. Phys. 118 (2015), 163301.
[23] J. Cui et al., Nucl. Instrum. Methods Phys. Res. Sect. B Beam Interact. Mater. At. 352 (2015) 104.
[24] R. Delaporte-Mathurin, et al., Sci. Rep. 11 (2021) 14681.
[25] L. Hu, et al., Surf. Sci. 626 (2014) L21.
[26] L. Hu, et al., J. Appl. Phys. 115 (2014), 173512.
[27] K.D. Hammond, et al., EPL Europhys. Lett. 110 (2015) 52002.
[28] H. Iwakiri, et al., J. Nucl. Mater. 283–287 (2000) 1134.
[29] F. Kong et al., Nucl. Instrum. Methods Phys. Res. Sect. B Beam Interact. Mater. At. 406 (2017) 643.
[30] N. Yoshida, et al., J. Nucl. Mater. 337–339 (2005) 946.
[31] N. Ohno, et al., J. Nucl. Mater. 438 (2013) S879.
[32] O. El-Atwani, et al., J. Nucl. Mater. 458 (2015) 216.
[33] O. El-Atwani, et al., Scr. Mater. 180 (2020) 6.
[34] R.W. Harrison, et al., J. Nucl. Mater. 495 (2017) 492.
[35] F. Zhu, et al., J. Nucl. Mater. 572 (2022), 154065.
[36] M. Ialovega, et al., Nucl. Fusion (2022).
[37] Z.J. Bergstrom, D. Perez, O. El-Atwani, Scr. Mater. 220 (2022), 114918.
[38] G. Renaud, R. Lazzari, F. Leroy, Surf. Sci. Rep. 64 (2009) 255.
[39] M. Thompson, et al., Nucl. Fusion 55 (2015), 042001.
[40] M. Thompson, et al., J. Nucl. Mater. 473 (2016) 6.
[41] K.h. Zakeri, et al., Surf. Sci. 604 (2010) L1.
[42] S.K. Tyler, P.J. Goodhew, J. Nucl. Mater. 74 (1978) 27.
[43] X. Yi, et al., Fusion Eng. Des. 125 (2017) 454.
[44] S. Kajita, et al., J. Plasma Fusion Res. 81 (2005) 745.
[45] G. Wulff, Z. Kristallogr – Cryst. Mater. 34 (1901) 449.
[46] J. Rahm, P. Erhart, J. Open Source Softw. 5 (2020) 1944.
[47] L. Vitos, et al., Surf. Sci. 411 (1998) 186.
[48] J. Wang, S.-Q. Wang, Surf. Sci. 630 (2014) 216.
[49] D. Scheiber, et al., Phys. Rev. B 101 (2020), 174103.
[50] J. Byggmästar, et al., Phys. Rev. B 100 (2019), 144105.
[51] A. Forslund, A. Ruban, Phys. Rev. B 105 (2022), 045403.